Terahertz Radiation Driven Chiral Edge Currents in Graphene

J. Karch,[1] C. Drexler,[1] P. Olbrich,[1] M. Fehrenbacher,[1] M. Hirmer,[1] M. M. Glazov,[2] S. A. Tarasenko,[2] E. L. Ivchenko,[2] B. Birkner,[1] J. Eroms,[1] D. Weiss,[1] R. Yakimova,[3] S. Lara-Avila,[4] S. Kubatkin,[4] M. Ostler,[5] T. Seyller,[5] and S. D. Ganichev[1]

[1]*Terahertz Center, University of Regensburg, 93040 Regensburg, Germany*
[2]*Ioffe Physical-Technical Institute, Russian Academy of Sciences, 194021 St. Petersburg, Russia*
[3]*Linköping University, S-58183 Linköping, Sweden*
[4]*Chalmers University of Technology, S-41296 Göteborg, Sweden*
[5]*University of Erlangen-Nürnberg, 91058 Erlangen, Germany*
(Received 19 July 2011; published 27 December 2011)

We observe photocurrents induced in single-layer graphene samples by illumination of the graphene edges with circularly polarized terahertz radiation at normal incidence. The photocurrent flows along the sample edges and forms a vortex. Its winding direction reverses by switching the light helicity from left to right handed. We demonstrate that the photocurrent stems from the sample edges, which reduce the spatial symmetry and result in an asymmetric scattering of carriers driven by the radiation electric field. The developed theory based on Boltzmann's kinetic equation is in a good agreement with the experiment. We show that the edge photocurrents can be applied for determination of the conductivity type and the momentum scattering time of the charge carriers in the graphene edge vicinity.

The "bulk" transport properties of graphene have been studied intensively in recent years and yielded insight into the half-integer and fractional quantum Hall effect, phase-coherent effects or spin transport on the micrometer scale, to name a few examples [1,2]. While the details of each of those effects depend crucially on the linear dispersion relation of graphene and its specific material properties, most of the transport phenomena have already been studied in other two-dimensional systems. Edge properties play an important role in transport of both graphene and other two-dimensional charge carrier systems—a prominent example is edge states in the quantum Hall regime—but microscopic edge properties cannot in general directly be extracted from bulk transport experiments. To explore edges in more detail one needs, for instance, to resort to scanning tunneling [3,4] or Raman scattering [5,6] experiments. The latter showed, e.g., that the scattering at graphene edges depends on the edge orientation. Here we demonstrate that chiral edge currents, generated by illuminating graphene edges with circularly polarized light, give information on edge properties, i.e., the momentum relaxation time close to the edge. The effect described here is probed in graphene; we note, however, that the effect is of general nature and should be observable also in other two-dimensional charge carrier systems.

In the experiments graphene is illuminated by terahertz (THz) radiation under normal incidence. In case of circularly polarized light the edge current is observed to form a vortex winding around the edges of the square-shaped samples. Its direction reverses upon switching the radiation helicity from left to right handed. Evidently, the photocurrent is caused by the local symmetry breaking at the sample edges resulting in an asymmetric scattering of carriers driven by the radiation electric field. It gives rise to a directed electric current along the sample boundary in a narrow stripe of width comparable to the mean free path. We show that the photocurrent measurements provide direct access to electron transport at the graphene edges and allow us to map the variation of scattering times along the edges.

We investigated two types of single-layer graphene samples: (i) large-area epitaxial graphene prepared by high-temperature Si sublimation of $4H$ and $6H$ polytypes of semi-insulating SiC substrates [7–9] and (ii) small area exfoliated graphene flakes [1] deposited on oxidized silicon wafers. Below, we report results on epitaxial graphene samples (labeled #1–$4H$, #2–$4H$, and #3–$6H$) and three samples prepared from exfoliated graphene. Hall measurements indicate that the epitaxial samples are n doped (due to charge transfer from SiC [7]) while the exfoliated samples are p doped. The measured carrier density lies in the range $(2$–$7) \times 10^{12}$ cm^{-2}, the Fermi energy E_F ranges from 200 to 300 meV and the mobility is about 1000 cm^2/V s at room temperature. Ohmic contacts were made at samples' edges (see, e.g., inset of Fig. 1).The resistance measured between different pairs of neighboring contacts in the large-area samples is ohmic and varies within less than 10%. Details on the material growth and characterization can be found in [10].

The experiments on edge photocurrents are performed applying alternating electric THz fields of a high power pulsed NH$_3$ laser [11–13] operating at wavelengths $\lambda = 90.5\ \mu$m, 148 μm or 280 μm (frequencies $f = 3.3$, 2, and 1.1 THz, respectively). The radiation induces indirect (Drude-like) optical transitions, because the photon energies are much smaller than the carrier Fermi energy. The
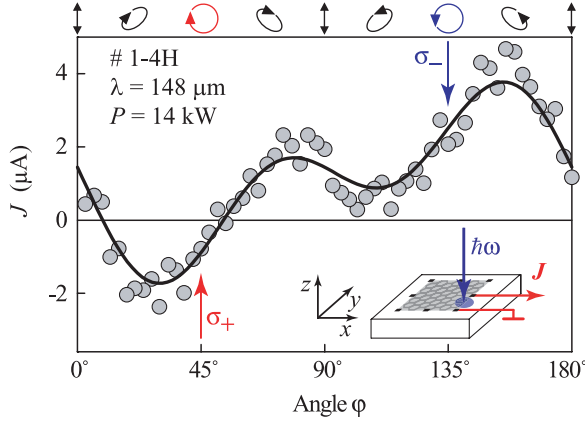
276601-1

FIG. 1 (color).   Photocurrent in sample #1–4*H* as a function of the angle φ defining the light polarization. Solid line is a fit to Eq. (1) [see also Eq. (7) and discussion]. The inset shows the experimental geometry. The ellipses on top illustrate the polarization states for various φ.

NH_3 laser generates single pulses with a duration of about 100 ns, peak power of $P \approx 10$ kW, and a repetition rate of 1 Hz. The radiation power has been controlled by the THz photon drag detector [14]. A typical spot diameter is from 1 to 3 mm. The beam has an almost Gaussian form, which is measured by a pyroelectric camera [15].

All experiments are performed at normal incidence of light and at room temperature. Elliptically and, in particular, circularly polarized radiation is obtained applying $\lambda/4$ quartz plates. The resulting polarization states described by the Stokes parameters [16]: S_1, S_2, and $S_3 \equiv P_{\text{circ}}$ are directly related to the angle φ between the initial linear polarization of the laser light along the y axis and the plate optical axis. The experimental geometry is shown in Figs. 1–3. The current is measured via the voltage drop across a 50 Ω load resistor.

Illumination of the edge of unbiased large-area samples between any pair of contacts results in a photocurrent. By contrast, if the laser spot is moved toward the center the signal vanishes. The detected signal depends strongly on the radiation polarization, Fig. 1. The principal observation is that for right- (σ_+) and left-handed (σ_-) polarizations, i.e., for $\varphi = 45°$ and $135°$, the signs of the photocurrent J are opposite. The overall dependence $J(\varphi)$ is more complex. It is well described by

$$J(\varphi) = J_A \sin 2\varphi + (J_B/2)\sin 4\varphi - J_C \cos^2 2\varphi + \xi$$
$$= J_A P_{\text{circ}}(\varphi) + J_B S_2(\varphi) + J_C S_1(\varphi) + \xi \quad (1)$$

and corresponds to the superposition of the Stokes parameters with different weights. The first term given by the coefficient J_A is just proportional to the radiation helicity, whereas the second ($J \propto J_B$) and third ($J \propto J_C$) terms change with degree and orientation of the linear polarization. Note that the observed offset ξ is usually smaller or comparable to J_A, J_B, and J_C (see Fig. 1). In our present

study we focus on the helicity driven photocurrent J_A. This is the only contribution which reverses the current direction upon switching the radiation helicity from σ_+ to σ_-. We also note that, for circularly polarized light ($P_{\text{circ}} = \pm 1$ and $S_1 = S_2 = 0$) and $\xi = 0$, the current is solely determined by the first term in Eq. (1). Therefore, it would be sufficient to measure the response to circularly polarized radiation. However, to increase the accuracy, we always measured the whole polarization dependence, like the one shown in Fig. 1, and extracted J_A by fitting Eq. (1) to the data.

To prove that the photocurrent is caused by illuminating the graphene edges, we scanned the laser spot across the sample along the y axis. The signal was picked up from a pair of contacts at the sample top and bottom edges aligned along the x axis. The experimental geometry and the photocurrent J_A versus the spot position are shown in Fig. 2. The current reaches its maximum for the laser spot centered at the edge and rapidly decays with the spot moving. Comparison of $J_A(y)$ with the independently recorded laser profile (dotted line) shows that the signal just follows the Gaussian intensity profile. This observation unambiguously demonstrates that the photocurrent is caused by illuminating the sample edges. Moreover,
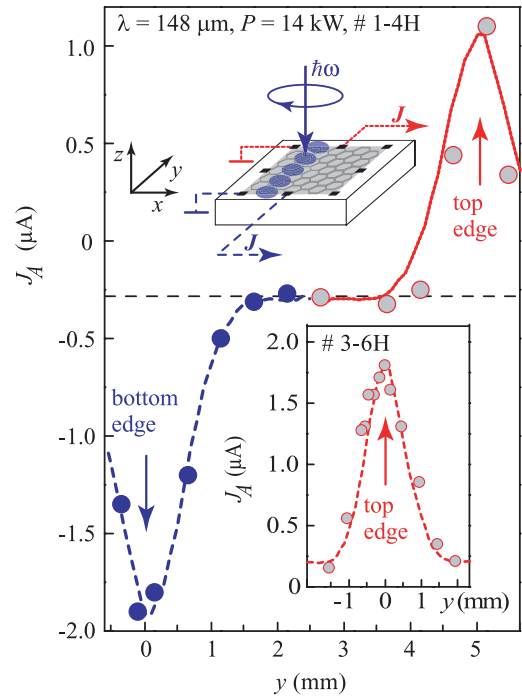

FIG. 2 (color).   Photocurrent J_A in sample #1–4*H* as a function of the laser spot position. The laser spot is scanned along y and the current is picked up from two contact pairs at the top (red circles) or bottom (blue full circles) sample edges aligned along x (see inset). Dashed lines represent the laser beam spatial distribution, which is measured by a pyroelectric camera, scaled to the current maximum. The bottom inset shows the scan for sample #3–6*H*.

Fig. 2 reveals that the helicity driven current J_A changes its sign for opposite edges.

The above results show that the current direction at a specific edge depends on the light helicity. To check this in more detail, we investigated currents excited by circularly polarized radiation for different pairs of contacts. Here, the laser spot is always centered between the contacts; see Fig. 3(a). The current direction for σ_+ (red arrows) and σ_- (blue arrows) circularly polarized radiation and the magnitude of J_A for various contact pairs are shown in Figs. 3(c) and 3(d). The figures document a remarkable behavior of the circular edge photocurrent: it forms a vortex winding around the edges of the square-shaped samples which reverses its direction upon switching from right- to left-handed. These dependencies are observed for all used wavelengths and samples. Helicity driven currents have also been observed for small area graphene flakes; see [10] for details. The origin of the vortex and the different photocurrent strength at different edges is discussed below.

The observation that a photocurrent occurs only if the laser spot is adjusted to an edge agrees with the symmetry
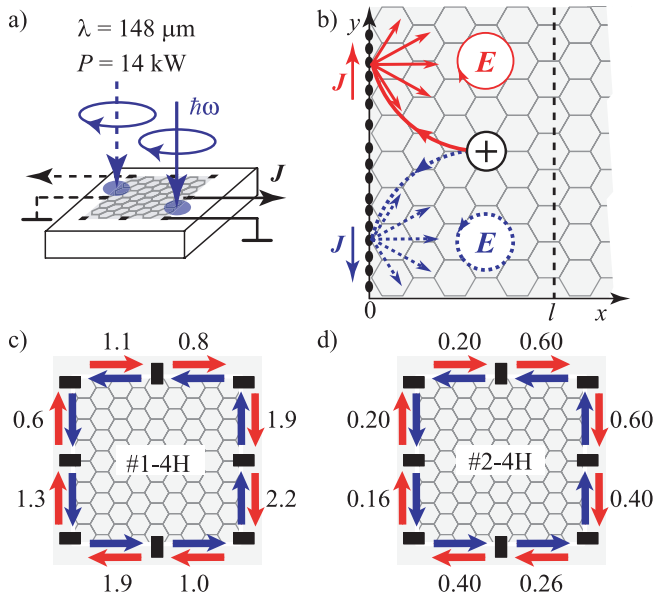

FIG. 3 (color). (a) Experimental geometry for the study of edge photocurrents. (b) Schematic illustration of the edge current generation. The electric field of circularly polarized radiation rotates clockwise or counterclockwise resulting in a circular motion of carriers, which is sketched by red and blue trajectories, respectively. Our theoretical model, see Eq. (7), shows that the circular edge current stems from carriers moving towards the edge. It is due to the *second order E*-field correction to the distribution function and involves the retardation of the electron motion with respect to the instantaneous electric field. Switching the radiation helicity reverses the motion direction and, consequently, the electric current. (c) and (d) photocurrent topology. Red and blue arrows show the current direction for σ_+ and σ_- polarizations, respectively, at $f = 2$ THz. Numbers indicate the photocurrent amplitude J_A in microampers.

analysis: In the ideal honeycomb lattice of graphene and for our experimental geometry, any photoelectric effect is forbidden [17], because the two-dimensional structure of graphene possesses a center of space inversion. Thus, the appearance of photocurrents at *normal* incidence of radiation is a clear manifestation of the symmetry reduction of the system, in our case, due to the edges. We also note that the typical photon energy $\hbar\omega \sim 10$ meV used in experiment is much smaller than the characteristic energy of carriers $E_F \sim 100$ meV. Thus, the mechanism of current formation can be treated classically and should involve the action of the light's electric field on free carriers in the vicinity of a graphene edge.

A microscopic process actuating the edge photocurrent generation is illustrated in Fig. 3(b). It involves the time dependent motion of carriers under the action of the electric field of circularly polarized radiation and scattering at the sample edge. We note that this mechanism is similar to that of the surface photogalvanic effect observed in bulk materials [18,19]. The microscopic theory of edge currents is developed in the framework of the Boltzmann kinetic equation. In this approach, the electron (hole) distribution is described by the function $f(\boldsymbol{p}, x, t)$. It depends on the carrier momentum $\boldsymbol{p}$, coordinate x ($x \geq 0$ for a semi-infinite layer), time t, and obeys the equation

$$\frac{\partial f}{\partial t} + v_x \frac{\partial f}{\partial x} + q\boldsymbol{E}(t)\frac{\partial f}{\partial \boldsymbol{p}} = Q\{f\}, \quad (2)$$

where $\boldsymbol{E}(t) = \boldsymbol{E}_0 e^{-i\omega t} + \boldsymbol{E}_0^* e^{+i\omega t}$ is the electric field of the radiation, $\boldsymbol{v} = v\boldsymbol{p}/p$ is the electron velocity, $v \approx 10^6$ m/s is the effective speed, q is the carrier charge ($q = +|e|$ for holes and $-|e|$ for electrons), and $Q\{f\}$ is the collision integral. The distribution function can be expanded in series of powers of the electric field,

$$f(\boldsymbol{p}, x, t) = f_0(\varepsilon_{\boldsymbol{p}}) + [f_1(\boldsymbol{p}, x)e^{-i\omega t} + \text{c.c.}] + f_2(\boldsymbol{p}, x) + \ldots,$$
$$(3)$$

where $f_0(\varepsilon_{\boldsymbol{p}})$ is the equilibrium distribution function with $\varepsilon_{\boldsymbol{p}} = vp$ being the electron energy, $f_1 \propto |\boldsymbol{E}|$, and $f_2 \propto |\boldsymbol{E}|^2$. The first order in $\boldsymbol{E}$ correction to the distribution function oscillates with frequency ω and does not contribute to a dc current. The directed electric current along the structure edge is, therefore, determined by the *second order E*-field correction f_2 and given by

$$J_y = 4q \int_0^\infty dx \sum_{\boldsymbol{p}} f_2(\boldsymbol{p}, x)v_y. \quad (4)$$

The factor 4 accounts for the spin and valley degeneracy.

We solve Eq. (2) and calculate the current, Eq. (4), for the simple form of the collision integral,

$$Q\{f(\boldsymbol{p}, x, t)\} = -\frac{f(\boldsymbol{p}, x, t) - f_0(\varepsilon_{\boldsymbol{p}})}{\tau}, \quad (5)$$

with τ being the scattering time, and the boundary condition at $x = 0$,

$$f(p_x > 0, p_y, 0, t)$$
$$= -\int \frac{v'_x}{2p'} f(\boldsymbol{p}', 0, t)\delta(\varepsilon_{\boldsymbol{p}} - \varepsilon_{\boldsymbol{p}'})\Theta(-v'_x)d\boldsymbol{p}', \quad (6)$$

corresponding to diffusive scattering. In the case of a degenerate gas, the edge current takes the form (see [10] for details):

$$J_y = -\frac{q^3\tau^3 v^2}{2\pi\hbar^2[1 + (\omega\tau)^2]}\left[\frac{10}{3}\frac{\omega\tau}{1 + (\omega\tau)^2} i[\boldsymbol{E}_0 \times \boldsymbol{E}_0^*]_z\right.$$
$$\left. + \left(1 + \frac{7}{6}\frac{1 - (\omega\tau)^2}{1 + (\omega\tau)^2}\right)(E_{0,x}E_{0,y}^* + E_{0,y}E_{0,x}^*)\right]. \quad (7)$$

The helicity driven current is given by the first term because $i[\boldsymbol{E}_0 \times \boldsymbol{E}_0^*]_z \equiv -P_{\text{circ}}$ for our geometry where the light propagates along $-z$. The second term yields the current caused by linearly polarized radiation and vanishes for circular polarization. In the case of elliptically polarized light, $E_{0,x}E_{0,y}^* + E_{0,y}E_{0,x}^* \propto (1/2)\sin4\varphi = S_2$. Both contributions are clearly detected in the experiment and correspond to the first ($\propto J_A$) and second ($\propto J_B$) terms in the empirical Eq. (1); see Fig. 1.

The helicity-dependent photocurrent described by Eq. (7) vanishes for zero frequency, has a maximum at $\omega\tau \simeq 0.6$ and decreases rapidly at higher frequencies. Exactly this behavior is found in experiment (see inset of Fig. 4) as we explain in more detail below. The only free parameter in Eq. (7) is the scattering time τ. Corresponding
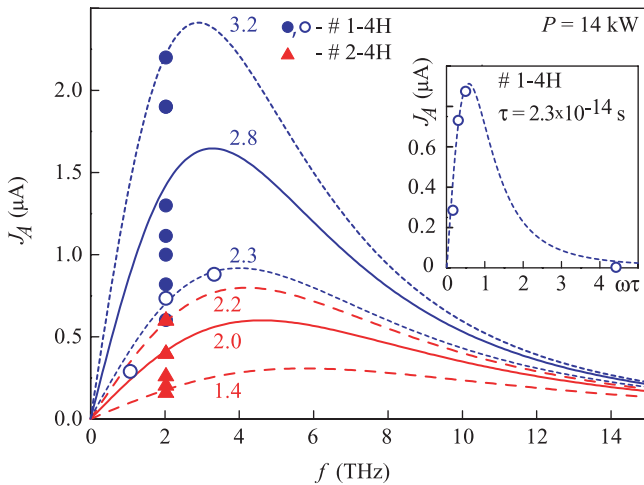

FIG. 4 (color). Photocurrent J_A measured for different edge segments. Lines are fits to Eq. (7). The fitting parameters $\tau/10^{-14}$ s for sample #1–4H and #2–4H are indicated by numbers. The inset shows the measured circular photocurrent $J_A(\omega\tau)$ at one of the edge segments of sample #1–4H (open circles) together with the fit after Eq. (7). Data point at $\omega\tau = 4.4$ is obtained applying a pulsed CO_2 laser.

data are shown in Fig. 4 where the photocurrent values measured at 2 THz for each of the contact pairs are plotted. These data points are first compared to calculated traces of J_A employing Eq. (7). Solid lines are calculated using the bulk values for the time τ extracted from resistivity and carrier density for samples #1–4H ($\tau = 2.8 \times 10^{-14}$ s) and #2–4H ($\tau = 2.0 \times 10^{-14}$ s). The bulk scattering times used in Eq. (7) give for some of the contact pairs already perfect quantitative agreement. For other edge segments the current deviates significantly. This is a consequence of the strongly nonlinear dependence of J_A on τ. Varying τ by only $\pm15\%$ changes the current by $\pm50\%$. By fitting the photocurrent J_A we can extract the local scattering time τ for every edge segment shown in Figs. 3(c) and 3(d). The best fits are shown by dashed lines in Fig. 4 and constitute a map of scattering times along the edge. Scattering times smaller/larger than the average bulk scattering time most likely reflect fluctuations of the local scattering time and hence inhomogeneities in the distribution of scatterers. The average value of the circular edge current scales with the sample mobility. To check the frequency dependence predicted by Eq. (7) we show in the inset of Fig. 4 J_A vs $\omega\tau$ for one edge segment using the extracted τ. The data points are perfectly described by Eq. (7) and confirm the model.

While the magnitude of the circular edge photocurrent agrees well with theory, the expected polarity of J_A for n-type graphene is opposite to the one observed. This, at first glance, surprising result agrees with results from spatially resolved Raman measurements indicating an enhanced density of p-type carriers at graphene edges [5,6]. This explains the sign of the photocurrent, which is generated in a narrow edge channel comparable to the mean free path (≈ 10–20 nm) and has opposite sign for electrons and holes; see Eq. (7). Actually, the difference in the conductivity type can be also understood from the details of the sample fabrication. It is well established that epitaxial graphene on SiC(0001) is n-doped due to charge transfer from the interfacial buffer layer (see, e.g., [7,8]), while so-called quasi-freestanding graphene, lacking such buffer layer and sitting on a hydrogen terminated SiC(0001) surface, is p doped [20]. Therefore, it is reasonable that the edges of epitaxial graphene, exposed to the SiC substrate without the interfacial layer, can be p doped. This assumption is corroborated by similar reports on the transition from n to p type of doping at the edges of graphene flakes on SiO$_2$, which were attributed to the difference in the work functions of graphene and the substrate [21].

To summarize, our observations clearly demonstrate that illuminating monolayer graphene edges with polarized terahertz radiation at normal incidence results in a dc edge current. The effect is directly coupled to electron scattering at the graphene edge and vanishes in bulk graphene. While the effect should exist in any two-dimensional charge carrier system the specific properties

of graphene, i.e., the high velocity of massless Dirac fermions, facilitate the experimental observation. Our results suggest that the circular photocurrents can be effectively used to study edge transport in graphene even at room temperature. An interesting aim for future research is to access the quantum regime where novel phenomena may occur [22].

[1] K. S. Novoselov *et al.*, Science **306**, 666 (2004).
[2] S. Das Sarma *et al.*, Rev. Mod. Phys. **83**, 407 (2011).
[3] Y. Niimi *et al.*, Phys. Rev. B **73**, 085421 (2006).
[4] K. A. Ritter and J. W. Lyding, Nature Mater. **8**, 235 (2009).
[5] C. Casiraghi *et al.*, Nano Lett. **9**, 1433 (2009).
[6] S. Heydrich *et al.*, Appl. Phys. Lett. **97**, 043113 (2010).
[7] K. V. Emtsev *et al.*, Nature Mater. **8**, 203 (2009).
[8] A. Tzalenchuk *et al.*, Nature Nanotech. **5**, 186 (2010).
[9] M. Ostler *et al.*, Phys. Status Solidi B **247**, 2924 (2010).
[10] See Supplemental Material at http://link.aps.org/supplemental/10.1103/PhysRevLett.107.276601 for details.
[11] S. D. Ganichev, S. A. Emel'yanov, and I. D. Yaroshetskii, JETP Lett. **35**, 368 (1982).
[12] S. D. Ganichev, Physica (Amsterdam) **273–274B**, 737 (1999).
[13] S. D. Ganichev and W. Prettl, *Intense Terahertz Excitation of Semiconductors* (Oxford Univ. Press, Oxford, 2006).
[14] S. D. Ganichev, Ya. V. Terent'ev, and I. D. Yaroshetskii, Pis'ma Zh. Tekh. Fiz. **11**, 46 (1985) [Sov. Tech. Phys. Lett. **11**, 20 (1985)].
[15] E. Ziemann *et al.*, J. Appl. Phys. **87**, 3843 (2000).
[16] B. E. A. Saleh and M. C. Teich, *Fundamentals of Photonics* (John Wiley & Sons, Inc., Hoboken, NJ, 2007).
[17] J. Karch *et al.*, Phys. Rev. Lett. **105**, 227402 (2010).
[18] L. I. Magarill and M. V. Entin, Phys. Solid State **21**, 743 (1979).
[19] V. L. Alperovich *et al.*, JETP Lett. **31**, 547 (1980).
[20] F. Speck *et al.*, J. Appl. Phys. **99**, 122106 (2011).
[21] E. J. H. Lee *et al.*, Nature Nanotech. **3**, 486 (2008).
[22] T. Oka and H. Aoki, Phys. Rev. B **79**, 081406 (2009); Z. Gu *et al.*, Phys. Rev. Lett. **107**, 216601 (2011); T. Kitagawa *et al.*, Phys. Rev. B **84**, 235108 (2011).